Soft Matter

Force fluctuations at the transition between quasi-static to inertial granular flow

Journal:	*Soft Matter*
Manuscript ID	SM-ART-06-2019-001111.R1
Article Type:	Paper
Date Submitted by the Author:	23-Sep-2019
Complete List of Authors:	Thomas, Amalia; University of Cambridge, Department of Applied Mathematics and Theoretical Physics Tang, Zhu; North Carolina State University College of Sciences, Physics Daniels, Karen; North Carolina State University, Department of Physics Vriend, Nathalie; University of Cambridge, Department of Applied Mathematics and Theoretical Physics; University of Cambridge, BP Institute

Soft Matter

ARTICLE TYPE

Cite this: DOI: 10.1039/xxxxxxxxxx

Force fluctuations at the transition between quasi-static to inertial granular flow

A. L. Thomas[a], Zhu Tang[b], Karen E. Daniels[b], N. M. Vriend[a]

Received Date
Accepted Date

DOI: 10.1039/xxxxxxxxxx

www.rsc.org/journalname

We analyse the rheology of gravity-driven, dry granular flows in experiments where individual forces within the flow bulk are measured. We release photoelastic discs at the top of an incline to create a quasi-static erodible bed over which flows a steady 2D avalanche. The flowing layers we produce are dense ($\phi \approx 0.8$), thin ($h \approx 10d$), and in the slow to intermediate flow regime ($I = 0.1$ to 1). Using particle tracking and photoelastic force measurements we report coarse-grained profiles for packing fraction, velocity, shear rate, inertial number, and stress tensor components. In addition, we define a quantitative measure for the rate of generation of new force chain networks and we observe that fluctuations extend below the boundary between dense flow and quasi-static layers. Finally, we evaluate several existing definitions for granular fluidity, and make comparisons among them and the behaviour of our experimentally-measured stress tensor components. Our measurements of the non-dimensional stress ratio μ show that our experiments lie within the local rheological regime, yet we observe rearrangements of the force network extending into the quasi-static layer where shear rates vanish. This elucidates why non-local rheological models rely on the notion of stress diffusion, and we thus propose non-local effects may in fact be dependent on the local force network fluctuation rate.

1 Introduction

Many studies of granular rheology have been developed by adapting classical fluid dynamics to granular-specific phenomena. In particular, non-local rheological models[1–3] aim to extend the fluidity observed in *local* regimes to regions in the *non-local* regime whose kinematic behaviour differs from that expected according to classical fluid dynamics. This reflects a need to better comprehend the physical mechanisms behind the transmission of forces within granular media, and their relation to rheological models. In this manuscript, we characterize the fluctuation rate of the force network as a key factor that granular rheology models must include, even though this feature is not present in classical fluids. Specifically, we use quantitative experimental measurements of inter-particle interactions to study how the stress tensor and its fluctuations differ across the boundary between two regions of the flow.

Granular systems have been classified based on the frequency and duration of inter-particle contacts[4–7]. A quasi-static system is reminiscent of a solid, a dense inertial flow resembles a fluid, and collisional (gas-like) states arise from the presence of highly energetic particles. Using dimensional analysis, granular flows can be classified into these three regimes via the dimensionless *inertial number*[8]

$$I \equiv \frac{\dot{\gamma} d}{\sqrt{P/\rho_0}}, \tag{1}$$

where $\dot{\gamma}$ represents the shear rate, d the particle diameter, P the pressure and ρ_0 the density of the particle material. It is useful to interpret the inertial number as the ratio between a microscopic timescale, $d/\sqrt{P/\rho_0}$, related to the time taken by particles to fall into a gap of size d under pressure P, and the macroscopic timescale given by $1/\dot{\gamma}$ linked to the plastic deformation of the material. Under these definitions, I is a local variable and its value roughly specifies the state of a granular system as being a quasi-static ($I < 10^{-3}$), dense inertial or intermediate ($10^{-3} < I < 1$), or collisional flow ($1 < I$)[9,10]. However, the thresholds that define each regime depend strongly on the geometry and may also vary depending on the choice of definitions for the constitutive variables[8,11].

Local granular rheology models[9,12] are based, as in classical fluid dynamics, on a constitutive relationship between a local stress tensor $\bar{\bar{\sigma}}$, and the corresponding the rate of shear strain tensor, $\bar{\bar{\mathfrak{J}}}$,

$$\bar{\bar{\sigma}} = P\bar{\bar{\mathfrak{J}}} + \frac{\mu P}{||\bar{\bar{\mathfrak{J}}}||}\bar{\bar{\mathfrak{J}}}. \tag{2}$$

The double-bar notation denotes second-order tensors and the

[a] Department of Applied Mathematics and Theoretical Physics, University of Cambridge, Wilberforce Rd, Cambridge CB3 0WA; E-mail: at682@cam.ac.uk.
[b] Department of Physics, North Carolina State University, Raleigh, NC, 27695, USA.

variable μ represents the ratio between shear and normal stress [13]

$$\mu = \frac{\tau}{P}, \tag{3}$$

where τ represents the shear stress.

Local models make use of an interpretation of the stress ratio μ as an effective friction coefficient depending solely on I [11]. This model would apply where the local shear stress is a function only of the local shear rate. In addition, by drawing an analogy between the stress ratio and the particle friction coefficient, local rheology models represent granular systems much like Bingham fluids, with an incipient yield stress ratio, μ_s. One popular model for the relationship $\mu(I)$ was successfully developed by Jop *et al.* [12]

$$\mu(I) = \mu_s + \frac{\mu_2 - \mu_s}{I_0/I - 1}, \tag{4}$$

where I_0 is a free parameter and μ_2 is the maximum stress ratio attainable by the system.

Local models have been shown to accurately describe a variety of experimental observations [9,12]. However, other scenarios have been identified where flow can exist in regions where the stress ratio is below the yield threshold, $\mu < \mu_s$. The basic assumptions of a local rheology fail to explain dynamic phase transitions [2,14], shear banding [15] or observations of creeping zones [3,16]. A wide range of phenomena, such as size-dependent flow thresholds [17], nozzle jamming at a finite opening [18,19], and secondary rheology [20,21] have been associated with *non-local* effects. Motivated by these shortcomings, non-local rheology theories aim to capture relationships between the stress tensor $\bar{\bar{\sigma}}$ and state variables in addition to the shear rate $\dot{\gamma}$. Several such models have been proposed [7,22–26], but for the moment there still lacks a universal theory that captures the fundamental physics behind the vast variety of non-local phenomena [27,28], and that is moreover well-posed [29,30]. In this work we focus on a particular cluster of models based on measures that are accessible to us.

Pouliquen and Forterre [31] proposed a description of non-locality based on processes activated by force-chain fluctuations. They suggested that the rate of rearrangements in the force network plays a similar role to temperature in thermal systems, rather than individual particle velocity fluctuations [32]. They proposed that the rate of plastic deformation proportionally affects the rate of generation of new random force networks within a granular flow.

Kamrin and Koval [1] used this principle to introduce the notion of local stress diffusion, whereby plastic events trigger other plastic events near them, within a lengthscale ξ, called the *cooperative length* of the plastic deformation mechanism. They proposed that the relevant variable was a *fluidity*, corresponding to the classical definition of the inverse of viscosity, $f \equiv \dot{\gamma}/\tau$. They additionally suggested that for granular materials the constitutive relationship for the granular fluidity g should be rescaled by the pressure under the definition

$$g \equiv \frac{\dot{\gamma}}{\mu}, \tag{5}$$

based on the argument that the collective, dynamic friction between particles that defines the shear stress between layers, τ, is expected to be pressure-dependent.

Finally, Bouzid *et al.* [2,3] took a related approach to modelling stress diffusion, noting that the cooperative motion of particles is both facilitated in the presence of more fluid neighbors, and suppressed when surrounded by a more solid neighbourhood. They therefore proposed that the fundamental definition of fluidity should be a *state variable*; g should be given by a coarse-grained field determined from the state of the system. They suggest several definitions for g, including (1) the difference between the number of contacts vs. sliding contacts per grain, and (2) the difference $\phi_c - \phi$ where ϕ represents the local volume fraction and ϕ_c the volume fraction at the limit $I \to 0$. In the end, they argue for simply using the inertial number I, because it increases with their concept of fluidity and becomes zero in the solid state. On the other hand, this choice requires the assumption of a quasi-incompressible system, which may not be satisfied for granular materials [9,30,33].

Several different microscopic variables have been used to describe non-local effects. For examples, Pouliquen & Forterre (2009) [31] described stress diffusion through stress fluctuations, Jop *et al.* (2012) [34] connected granular fluidity (as the inverse of viscosity) to the standard deviation of the strain-rate tensor, and Zhang & Kamrin (2017) [35] proposed and confirmed that granular fluidity can be fundamentally described in terms of only velocity fluctuations, δv, and packing fraction, ϕ, as

$$g = \frac{\delta v}{d} F(\phi), \tag{6}$$

where d is the particle diameter and F is a function that defines the dependency of g with ϕ.

In this paper we make direct observations of the forces that cause localised rearrangements in areas where no motion would be expected according to local rheology models. We aim to use our insight into the force network to investigate the physical mechanisms that drive non-local effects in experiments at low-intermediate values of I where such non-local effects are becoming relevant. In addition, we test whether the shear rate is an appropriate variable in the description of fluidity at all, given that even for static granular packings, force chain configurations are not solely determined by particle positions [36,37]. Instead, there is a force network ensemble (FNE) which can fluctuate independent of, and in addition to, particle rearrangements under shear. Therefore, we additionally consider some alternatives for defining the fluidity g.

Our experiments are performed in the apparatus described in Thomas and Vriend [38], which is capable of making quantitative measurements of both the flow field and the stress field within 2D free-surface flows, using photoelastic discs as the granular material. We examine the rheology of such flows at low to intermediate-I, by taking high-speed video that allows for photoelastic measurements of inter-particle forces [39,40]. The flows consist of a $\sim 12d$ deep layer of particles flowing in a dense inertial regime over a quasi-static layer that is $\sim 5d$ to $6d$ deep, providing data in a regime close to the transition between quasi-static and dense inertial flows.

We report coarse-grained profiles of each of the candidate rhe-

ological variables that characterise the state of the granular system under investigation. We are thereby able to directly measure the force chain fluctuation rate and compare its behaviour to the shear rate, allowing for experimental tests of the models proposed in the three non-local rheologies[1,2,31], as well as confirming whether the force chain fluctuations are able to identify the value of μ_s[41]. We conclude that the force-chain fluctuation rate may provide a local representative of granular fluidity, an effect beyond simply using stress diffusion to explain non-local effects.

2 Experimental methods

2.1 Apparatus

Figure 1 shows a diagram of the experimental setup, in which photoelastic discs are released to produce 2D avalanches. The chute is bounded by two large acrylic panels with a fixed separation of 8 mm, providing enough space to allow the discs to roll freely with minimal resistance but without toppling. Along the base of this channel, we clamp a plastic strip with semi-discs of alternating 12 and 21 mm diameters to provide basal roughness. The complete setup is just over 3 m high and 3.5 m long, and permanently inclined at an angle of 20° above the floor.

We cast photoelastic discs with diameters of 11, 12 and 13 mm (equal numbers) and a thickness of 6 mm from Clear Flex 50 (polyurethane from Smooth-On, Inc.) using the technique developed by Barés[42], Barés *et al.*[43], Abed Zadeh *et al.*[44]. The discs produced have density $\rho_0 = 1120$ kg/m^3, Shore A hardness 50, and exhibit slight viscoelastic behaviour[45]. The photoelastic material used is softer than is typically found in nature and industry, but we assume particle stiffness does not have a significant effect on the flow rheology[46]. By introducing a small (10%) polydispersity, we are able to suppress crystallisation[47], without causing size-segregation. In the following calculations, the average diameter $d = 12$ mm is used.

At the start of each experiment, well-mixed discs are placed into the hopper above the chute upper end and then released by manually sliding a plastic gate at the base of the hopper. We measured that the flow released from the hopper produces an approximately a constant flow rate. The particles fall into the channel formed by two 2 m-long and 0.5 m-high acrylic sheets, and avalanche down the incline.

Releasing the gate simultaneously triggers a Phantom v2012 Ultrahigh-Speed Camera (Vision Research) to record the flow of photoelastic discs at a downstream distance of 25 cm from the hopper opening. Images are collected at 1000 frames per second with a $1/8000$ s exposure time, while backlit illumination is provided by a TruOpto OSPM-R5030ETS Red LED. The imaging region contains a pair of oppositely-polarized circular polarizers for making photoelastic measurements of the interparticle forces. A sample image, showing the force chains as light streaks against a dark background, is shown in the central region of Fig. 1. After an initial acceleration of the avalanche leading edge, and before the depletion of the hopper, the flow is in a steady state. We focus our attention on this interval, which is characterised by a constant flow height and velocity profile. While we collect up to 3000 frames (3 s) of flow, due to the computationally-intensive analysis (see §2.2) we only consider 500 frames (0.5 s of flow, which satisfies a representativity test) for each of four experimental runs.

The experimental setup is designed so that the rolling discs have on average 1 mm leeway on either side. In addition, the discs are lightly coated in flour to lubricate the interaction with the acrylic side-walls. Friction between the discs and side-walls is large enough to affect the flow velocity profile, but not enough to induce a visible photoelastic response[38]. As a result, side-wall friction does not affect the photoelastic force measurements.

We determined the yield stress ratio μ_s of the particles using the method described in Tang *et al.*[41]. This apparatus allows both continuous shearing from the inner wall and simultaneous measurement of τ and P. Because the stress ratio μ approaches μ_s for very slow inertial numbers, the largest values of μ obtained for a very slow rotation rate (10^{-3} d/s at the inner wall) provide an estimate of μ_s. We found this to be approximately 0.26 ± 0.01 for our particles, which is consistent with measurements of other circular particles in the same apparatus.

2.2 Imaging particles and forces

The experimental technique applied in this study is based on the material property of *photoelasticity*, by which certain materials become birefringent to a degree sensitively dependent on the magnitude of external loads[48]. As a consequence, light that travels through a photoelastic material under stress experiences a change in its polarisation. When placed between a pair of opposite polarising sheets, the fringe patterns produced by the light transmitted through the system can be related to the magnitude and direction of the load applied to the material. Thus, the forces that would produce a specific fringe pattern are determined via an iterative optimisation algorithm (Levenberg-Marquardt). We use a force-measuring code built on the open-source program PeGS[39,40] but without relying on particles being force-balanced, as this is not applicable in our dynamic system.

We use the Matlab function *imfindcircles* (Hough transform) in post-processing to find circles in each experimental image. Because of the high frame rate, the circles identified are easily tracked throughout the experiment. Depending on the specific particle edge visibility and the instantaneous photoelastic pattern brightness, we estimate a location error of at most 1 mm, or $\approx 10\%$ of the mean diameter.

We determine, from the data collected during the particle tracking, that the coordination number of the system is 4.2 ± 0.3. Only a small proportion ($< 30\%$) of the total particles take part in the force network. The wide black gaps between force chains are filled with "rattlers"; particles instantaneously not exhibiting an obvious photoelastic response to any force. The proportion of discs involved in the force network increases with depth, but in the experimental frames analysed no less than 70% of discs fail to produce a visible photoelastic pattern. Given that the average disc mass is 0.78 g, only forces that are at least three times greater than the average disc weight will produce a visible photoelastic

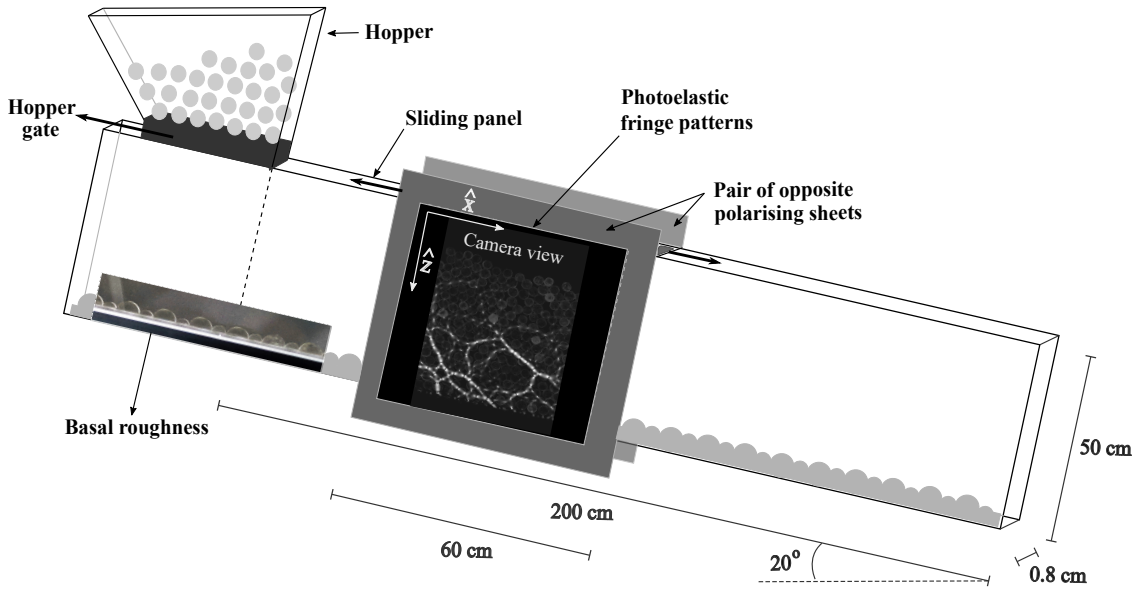

Fig. 1 Schematic of the experimental apparatus[38] used to create and monitor 2D flows of photoelastic discs. On opening the hopper gate, a 2D avalanche of discs rolls down the incline. The resulting flow is recorded by a high-speed camera as it passes in steady state between a pair of opposite polarizers, which allow the visualisation, and later quantification, of instantaneous inter-particle forces.

response[38], which rules out a great majority of the contacts as bearers of significant loads. On the other hand, discs that are involved in force chains carry loads that are on average at least an order of magnitude larger than the minimum. Henceforth, it is important to be aware that a large number of small forces are being neglected in the following analysis, as the technique sensitivity sets a threshold to the contacts considered to form part of the force-network.

For those discs that do exhibit a photoelastic response, we crop out the fringe patterns from the experimental images to solve the inverse problem using PeGS[39,40]. In Thomas and Vriend[38] we evaluated the technique's force measurement error and its dependency on the number of forces acting on a disc, z. As reported in that paper, we estimate that the sensitivity lower bound of our photoelastic measurements is $0.02\ N$. This value depends on the inherent photoelastic response of Clear Flex 50, the thickness of the discs, and the image resolution. In addition, a systematic error of $0.05N$ exists for forces of magnitudes smaller than $0.5N$. On the other hand, the random error of the technique can be as large as 20% between the lower bound of $0.02\ N$ and a critical value that depends on the number of forces acting on the disc, z. The reliability of the force measurements drops significantly when the loads on the discs exceed $2.5\ N$ when $z=2$, $1.6\ N$ when $z=3$ and $1.2\ N$ when $z=4$. The limits of the technique lie in the resolution of the experimental images (due to camera resolution and diffusion in the photoelastic material) and in the trade-off between computational cost and accuracy.

The outcome of running the selected frames through PeGS is a list per frame of tracked discs. Each disc is assigned a unique ID number, its coordinates, radius, velocity magnitude and direction, and a list of force vectors acting on the disc. Each force in this vector is described in terms of its magnitude, direction, point of application, and the ID of the adjacent disc that applies each load.

2.3 Coarse-graining

To obtain continuous profiles from the list of discrete experimental results, we applied a coarse-graining technique based on the work of Goldhirsch[49] and Weinhart *et al.*[50] to create continuum fields from discrete data. They propose coarse-graining expressions for density profiles $\rho(z)$, downstream velocity $V_z(z)$, and the four stress tensor components, $\sigma_{xx}(z)$, $\sigma_{xz}(z)$, $\sigma_{zx}(z)$ and $\sigma_{zz}(z)$. The main technique is to define a coarse-graining function for any quantity, $\mathcal{W}$, such that the contribution from a disc at any point a distance r from its centre, using a coarse-graining length-scale w, is:

$$\mathcal{W}(r,w) = \begin{cases} C\exp\left[\frac{-1}{1-|r_i/w|^2}\right] & r < w \\ 0 & r \geq w, \end{cases} \tag{7}$$

where C is a normalisation factor to obtain the total volume of $\mathcal{W}$ over the whole domain.

This particular vector function was chosen because it approaches zero as $r \to w$ and it provides an interpretation of the coarse-graining length-scale based only on w. The function $\mathcal{W}$ spans over an ellipse of height and width equal to the vertical and horizontal coarse-graining lengths. $\mathcal{W}$ depends on the distance to the centre of each disc, $|\mathbf{r}-\mathbf{r}_i|$, relative to a predefined coarse-graining length-scale w. The length-scale w needs to be specified for each system[49,50], and may have different components in the vertical and horizontal directions (here, w_z and w_x, respectively).

We notice that the flow does not change significantly in the stream-wise direction (horizontal, $\hat{x}$), while it does vary rapidly in the cross-flow direction (vertical, $\hat{z}$), so we choose different values for w_z and w_x. We use $w_x = 5d$, as this defines the width of the section of the experimental image where the circle finding is most accurate (due to small changes in the background illumination close to the viewing window edges). For the experiments described in this paper, the optimal vertical coarse-graining length-scale was

found to be $w_z = 3d$, selected by finding the smallest value that obtains smooth packing fraction profiles. Note that these values also place a limit on how close to the boundaries we are able to make measurements. In the plots that follow, all values measured within $(3d)$ of the vertical boundaries of the images are shown by either dotted lines or lighter colors. We estimate the location of the free surface as the line that best fits the highest points of the discs in the topmost layer, and then we truncate the profiles below the base and above the free surface.

3 Flow characterisation

We measure the density profile $\rho(z)$ according to Goldhirsch [49] from discrete particle tracking measurements using Eq. 7, and use this to measure the packing fraction profile $\phi(z) = \rho(z)/\rho_0$. As previously observed for this apparatus [38], we find that $\phi(z) \approx 0.81 \pm 0.07$, which is a slightly lower than random close packing ($\phi_{RCP} = 0.84$ [51,52]). Louge *et al.* [53] have reported low packing fractions in the upper flowing layer, but the value we measure is uniform (within our experimental error) along the whole profile, in both quasi-static and upper flowing layers. Although we measure no significant variations in ϕ with depth, we observe that all layers are equally spaced from each other by $0.9d$ [38,54], but that the degree of layering becomes less pronounced closer to the free surface. It is possible that the packing fraction indeed decreases towards the free surface, but by an amount smaller than the experimental error or is dampened by coarse-graining.

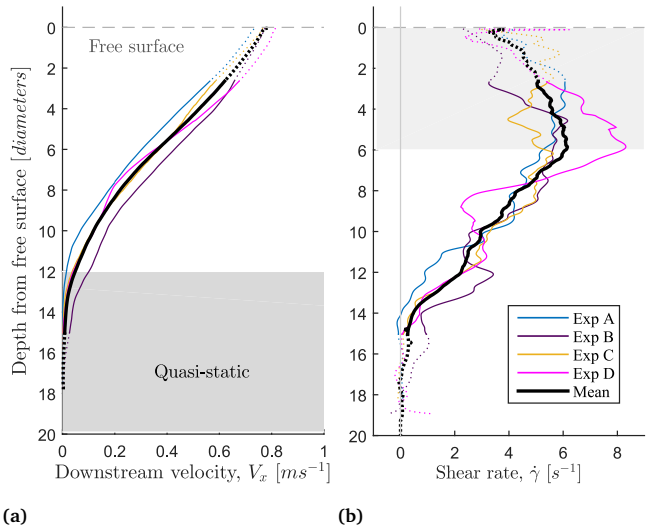

Fig. 2 (a) Coarse-grained downstream velocity profile $V_z(z)$, and (b) mean flow shear rate profile $\dot{\gamma}(z)$ of the steady flow measured at a distance 25 cm from the hopper opening, with individual runs aligned to have $z = 0$ at the free surface. The gray shades denote regions of different observed behaviour. On (a) the shaded region contains quasi-static particles, as opposed to the flowing layer above. On (b) the region shaded in light gray shows shearing rates decreasing with particle velocities, perhaps related to a decrease in packing fraction, too small to measure directly.

For each of the four experimental runs, the flow thicknesses H are between $17d$ and $20d$, but differ primarily in the amount of material that accumulates as a quasi-static basal layer. Therefore, in the plots below we examine the properties of the flows as a function of the vertical coordinate z, as measured with the origin placed at the free surface [55]. As shown in Figure 2a, we observe that the four downstream velocity profiles, $V_z(z)$, are consistent in their shape and magnitude.

A quasi-static layer forms below a depth of about $12d$. In Figure 2a, we shade the area where the particles move up to 100 times slower than their free surface counterparts. Along the whole chute, this quasi-static layer forms a super-stable heap that is thickest closest to the hopper, and decreases to zero thickness at the lower, open end of the chute [38]. For our particular system, the super-stable heap effectively increases the inclination of the steady-state flow above it by 5°. As in other reports of experiments where super-stable heaps form in narrow channels [56–60], we observe quasi-linear velocity profiles in the flowing layer, $0d < z < 12d$.

Using the mean velocity profile, taken across all four runs, we calculate the shear rate $\dot{\gamma} = dV_x/dz$ by taking second order central finite differences. The resulting profile $\dot{\gamma}(z)$ is shown in Figure 2b. We observe that it obtains near-zero values in the quasi-static bottom layer, and gradually increases in the transition to the flowing layer. A maximum value of $\dot{\gamma} = 6$ s^{-1} is reached at a depth of approximately $6d$. A decrease close to the free surface, in the region shaded light gray in Figure 2b, is surprising given that we observe uniform packing fraction throughout the flow. However, as the depth of maximum shear rate ($z = 6d$) is below the cut-off of boundary effects on the coarse-graining ($z = 3d$), we accept it as a physical phenomenon. However, it is possible that our measurements of the packing fraction ϕ within this region are overestimated by an amount smaller than our experimental error. If so, a slightly smaller ϕ can still cause significant differences in the shear rate. Even though this region is not in the collisional state where the packing fraction would be expected to decrease much more dramatically, we interpret this region to be transitioning to a high-I state.

We calculated the continuous stress tensor components σ_{ij} from discrete force measurements according to the technique proposed by Weinhart *et al.* [50]. The coarse-grained profiles $\sigma_{ij}(z)$ are shown in Figure 3a. The absolute values of the profiles have a large systematic error [38], particularly towards the top of the flow, where the proportion of small forces below the experimental technique sensitivity is largest. However, the gradients in σ_{ij} coincide with the expected hydrostatic increase with depth of the normal and shear stresses. It follows that the stress ratio μ, as defined by Equation 2, is constant in the dense flow region. In contrast, we observe μ decreases with depth below the boundary with the quasi-static layer. Interestingly, μ does not fall below the measured value of $\mu_s \approx 0.26$, which is observed to be reached only at the base. Figure 3b raises the interesting question of whether we do not observe non-local regions, where $\mu < \mu_s$, because the quasi-static region is not deep enough to reach it. These results are consistent with previous analyses [59,61,62] on the impact of side-wall friction on the rheology of flows in narrow channels. As the pressure on the side-walls increases with depth, so do the frictional forces at the walls. In consequence, μ is predicted to

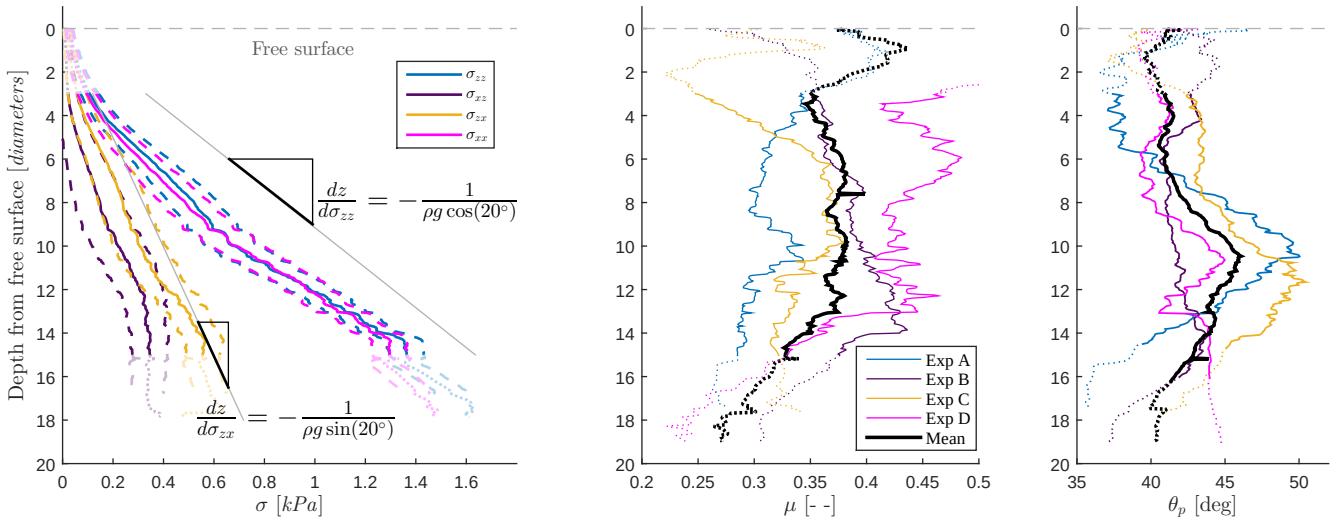

(a) Magnitudes of the stress tensor component. **(b)** Stress ratio as defined in Equation 2 **(c)** Principal orientation.

Fig. 3 Analysis of the stress tensor coarse-grained according to Weinhart *et al.* [50]: (a) The solid coloured lines represent each of the four stress tensor components, coarse-grained and averaged over the four experiments, while the dashed lines delimit the error bounds. The straight gray lines show the gradients expected in the case of hydrostatic pressure and shear; (b) the shear ratio and (c) the principal orientation obtained from the profiles shown in (a), for each experiment (coloured lines) and their mean (solid black line). Values within $3d$ of the free surface or base are plotted in dotted lines and light colours as their measurements are affected by proximity to a boundary.

decrease with depth from the free surface.

The principal stresses show a change of direction, measured via the principal orientation, θ_p [38], shown in Figure 3c. The peak in θ_p coincides in position with the transition between static and flowing layers. This peak is on average 5° larger than the value of θ_p measured close to the free surface and bottom boundary. Incidentally, 5° is the angle the flowing layer velocities make to the base, as the super-stable heap that forms at the chute base effectively increases the inclination of the flowing layer by this amount. In other words, we observe a 5° angle forms between the velocity components V_x and V_z in our frame of reference aligned with the setup inclination.

Since we now have experimental coarse-grained measurements for the pressure P from the symmetric component of our measured $\bar{\bar{\sigma}}$, we calculate a profile for the inertial number I, defined in Equation 1, with depth. This plot of the experimental results is shown in blue in Figure 4. We find that the inertial number decreases steadily with depth from the free surface within the flowing layer. However, in the quasi-static layer where the shearing effect of the rough base is expected to be most important, the shear rate approaches zero, and therefore so does I.

With profiles for both μ and I, we investigate the relationship between them. By plotting them against each other in Figure 5, we see a rapid increase of μ at low values of I, and a plateau at the maximum value of μ_s. These are characteristics modelled by Jop *et al.* [12] in Equation 4. A fit of this $\mu(I)$ model to the experimental data, fixing $\mu_s = 0.26$ (measured separately using the apparatus described by Tang *et al.* [41]), is shown in red in Figure 4, and obtains $I_0 = 0.004$ and $\mu_2 = 0.376$.

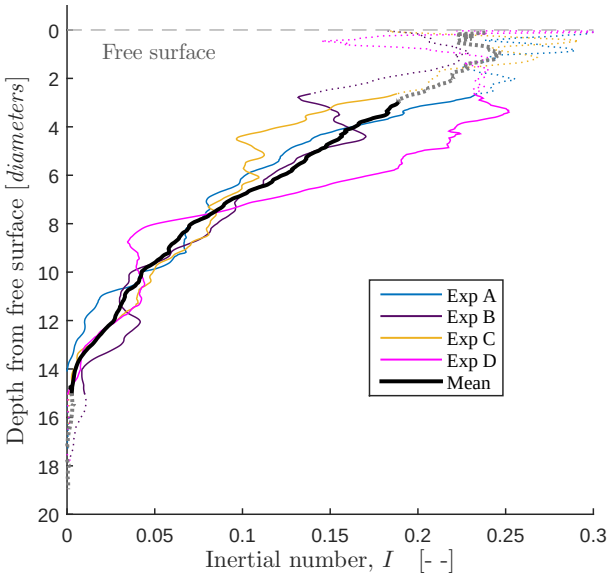

Fig. 4 Profile $I(z)$ of the inertial number, as defined in Equation 1. Data collected at distances within a coarse-graining length $w_y = 3d$ of the free surface and chute base are shown with a dotted line, as these points are affected by proximity to the boundaries.

4 Results

4.1 Force network fluctuations

It has previously been observed that spatial and temporal fluctuations in the interparticle forces provide a measure of how close/far a system is from the boundary between flowing/non-

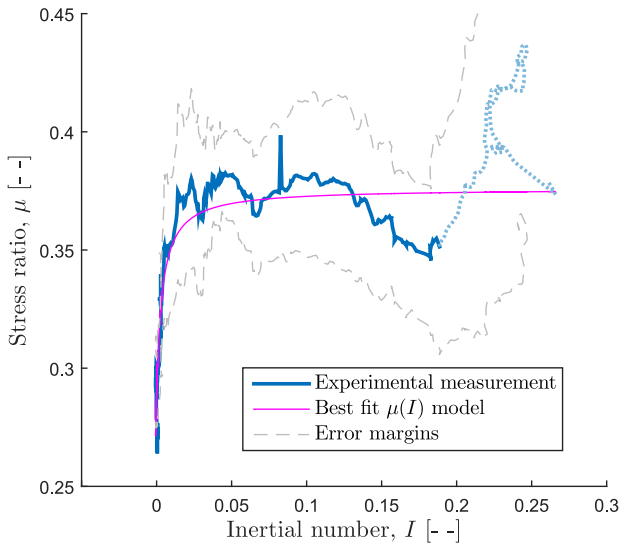

Fig. 5 Measured values of μ (Figure 3b) as a function of the corresponding values of I (Figure 4), plotted in blue. The light gray dashed lines denote the experimental error margins. The red line shows the best fit of the $\mu(I)$ model proposed by Jop *et al.*[12] (Equation 4), for a fixed $\mu_s = 0.26$, and fitted $\mu_2 = 0.376$ and $I_0 = 0.004$. Data collected at distances within a coarse-graining length $w_y = 3d$ of the free surface and chute base are shown in dotted lines, as these points are affected by proximity to the boundaries.

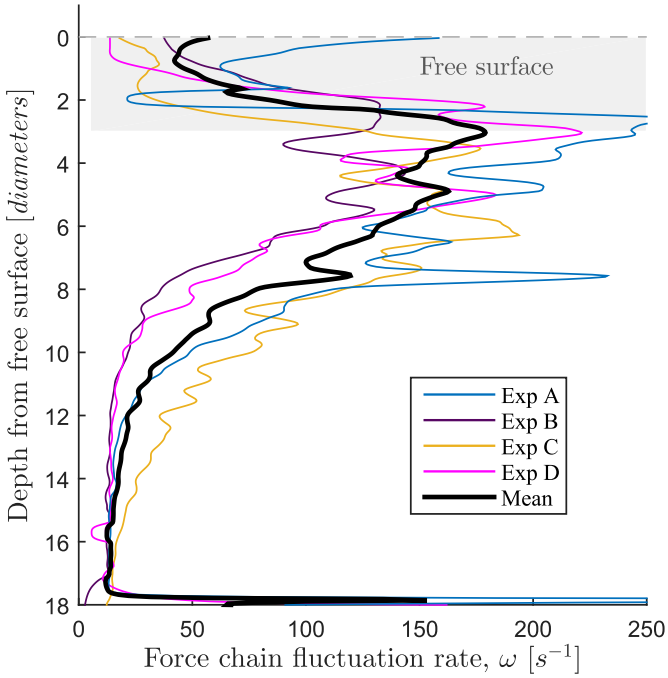

Fig. 6 Profile of the pixel brightness fluctuation frequency, representative of the force-chain rearrangement rate. Each colour represents the coarse-grained result of a different individual experiments, and the thick black line shows their average.

flowing regions or regimes[41,63,64]. In order to identify whether this effect is an important factor in nonlocal rheology[1,2,31], we make similar measurements for our avalanching flows. To measure the duration of time that a particular point in the flow maintains the same forces, we treat each pixel brightness as an individual time series $B(t)$. In our flows, the particles only rarely have more than one photoelastic fringe. Therefore, a growing or decaying brightness approximately quantifies the growth or destruction of a force chain.

For each pixel, we measure the autocorrelation coefficient $C(\Delta t)$ across the entire time series:

$$C(\Delta t) = \frac{\sum_t \left[B(t) - \bar{B}\right]\left[B(t+\Delta t) - \bar{B}\right]}{\sum_t \left[B(t) - \bar{B}\right]^2}. \quad (8)$$

We observe that these are well-fit by a function of the form $C(\Delta t) \propto \exp[-\Delta t/T]$, where T represents the typical lifetime of a force chain at that depth. At each depth, we average all such measurements of T to determine a typical lifetime of force chains, and report these values as a fluctuation rate $\omega \equiv 1/T$. The resulting $\omega(z)$ observed for each of the four runs are shown in Figure 6, along with their average. This analysis quantifies our visual observation that force chains are reconfiguring faster close to the free surface of the flow ($z = 0$).

Several features of Figure 6 stand out. First, we bear in mind that only forces that are about an order of magnitude greater than the average disc weight produce a measurable photoelastic response. For this reason pixels corresponding to discs in the top few layers may not reach maximum intensities, and often will not display intensity variations at all. Secondly, the location of the free surface is measured by averaging the highest points of the discs that we track on the free surface throughout the duration of the steady state flow. Occasionally the flow is thinner than the mean flow thickness H, so at these times pixel intensities do not vary significantly. We thus strongly suspect that the results shaded in light gray in Figure 6, extending up to a depth of $3d$ are underestimated.

Below a depth of $3d$, ω decreases with depth, which coincides with the direct observation of force chains fluctuating faster at the top of the flow. However, even within the quasi-static region, at depths of at least $12d$ according to Figure 2a, ω remains larger than zero. This implies that the force network rearranges even when particle positions do not change at all, epitomizing the ensemble of force configurations for a given configuration[36,37].

Using the profile $\omega(z)$, combined with $\dot{\gamma}(z)$ reported in Figure 2b, we can now test the proposal by Pouliquen and Forterre[31] that the rate of plastic deformation is proportional to the rate of generation of new random force networks within a granular flow. As shown in Fig. 7, we observe that within the region in intermediate-I regime ($3d < z < 12d$) the relationship between $\dot{\gamma}$ and ω is indeed approximately linear[32]. However, we also observe that for low shear rates ($\dot{\gamma} < 2$ s^{-1}), ω plateaus at a minimum value of approximately 20 s^{-1} rather than continuing to decrease to zero. This result is linked to the previous observation that force chains fluctuate even within the quasi-static region, where shear rates are practically zero. The force network fluctuations[36] decrease slowly with distance from the boundary between flowing and static layers. We believe the lengthscale where we measure force chain rearrangements in the quasi-static

region is indicative of the lengthscale at which non-local effects may be observable.

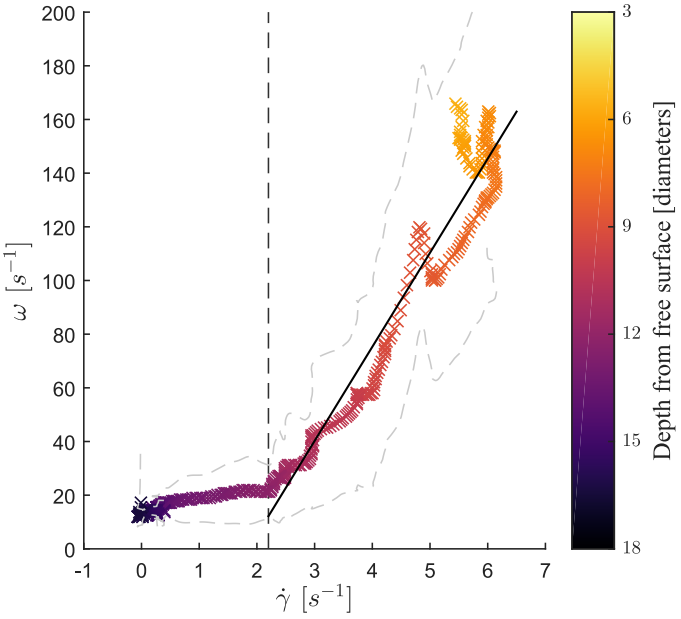

Fig. 7 Parametric scatter plot of $\omega(z)$ and $\dot{\gamma}(z)$ using the data shown in Figures 6 and 2b. The colour of each experimental point represents the depth at which the data was taken. The light gray dashed lines denote the experimental error margins. The dark gray dashed line separates the points collected at depths larger than $12d$, in quasi-static state (left of the line), with those obtained in the flowing layer (right of the line). The solid gray line shows a linear regression (correlation coefficient $R = 0.97$) for $3d < z < 12d$, the region interpreted to be in the intermediate-I regime.

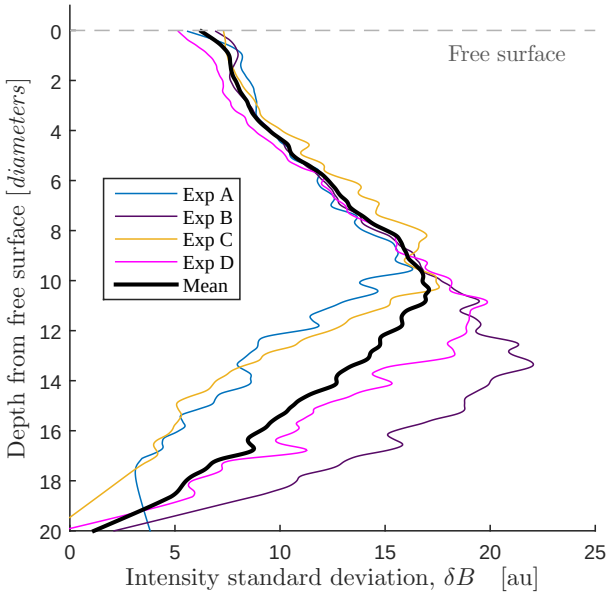

Fig. 8 Profile of the horizontally-averaged pixel intensity standard deviation, as defined by Tang *et al.*[41]. They interpreted the position of the peak is indicative of $\mu = \mu_s$, but here the peak in δB is found at an approximate depth of $10d$, where $\mu > \mu_s$. Each colour represents the coarse-grained result of a different individual experiments, and the thick black line shows their average. Data collected at distances within a coarse-graining length $w_y = 3d$ of the free surface and chute base are shown in light colours and dotted lines, as these points will be affected by proximity to the boundaries.

Tang *et al.*[41] observed that a sharp change in the force chain fluctuations, quantified via δB (the standard deviation of B), identified the location in the flow at which μ dropped below μ_s. As shown in Fig. 8, we compute how δB varies as a function of depth. While we observe a distinct peak in $\delta B(z)$, at a depth of $10d$ below the free surface, this location does not coincide with the depth at which $\mu = \mu_s = 0.26$. As recorded in Figure 3b, the μ threshold is crossed quite close to the base, at a depth below $18d$. Therefore, this peak is not the same feature reported in[41]. Instead, this feature likely arises through two limiting effects: particles near the top have low δB because they sustain only small forces, while particles at the bottom have low δB because they are not flowing (small ω). Between these two extremes, there is therefore is a peak value. Plots of $\delta B/B(z)$ have also been considered, and they show a peak at the same depth.

4.2 Evaluating granular fluidity proposals

In Figure 9, we compare the behaviour of (purple/darkest line) the granular fluidity $g = \dot{\gamma}/\mu$ (Eq. 5), defined in analogy to classical fluids as the inverse of viscosity, with (blue/intermediate shade line) that of the inertial number I, and finally with (orange/lightest line) the quantity presented in the previous section, the force fluctuation rate ω.

Each of the regimes introduced so far have been demarcated by the grayscale background. From the bottom up: (1) quasi-static from $z > 12d$ (darkest shading) identified from the mean downstream velocity V_x shown in Figure 2a; (2) intermediate-I, dense flow regime from $12d > z > 6d$ identified from packing fraction and velocity measurements; (3) still intermediate-I regime for $6d > z > 3d$, but although we do not observe significant variations in the packing fraction within the flowing layer, we noticed a change in the behaviour of the shear rate, $\dot{\gamma}$ (Figure 2b). This may be due to a very slight change in the packing fraction smaller than our experimental error, that may still affect $\dot{\gamma}$. If so, we interpret the flow within the range $6d > z > 3d$ to be slowly transitioning to a collisional state. (4) nearly-collisional surface flow from $3d > z > 0d$ (lightest shading) is the region within which the free surface fluctuates in position and ω values are underestimated.

Within the heap at the bottom, motion occurs as sporadic, localised rearrangements of small clusters of particles. Under an assumption that this region should have zero fluidity because velocities are small and discontinuous, then g and I could be considered as describing the granular fluidity within this region, since both g and I are accordingly nearly zero for $z > 12d$. However, we instead interpret that, because in our experiments the force chains fluctuate within what is in fact a not closely-packed *quasi*-static flow, the fact that particles *may* move should imply a fluidity that, like ω, is appropriately non-zero. Estep and Dufek[65] also reported significant force network rearrangements within a small, confined erodible bed over which a similar 2D avalanche of photoelastic discs flowed. Having studied a closely and tightly

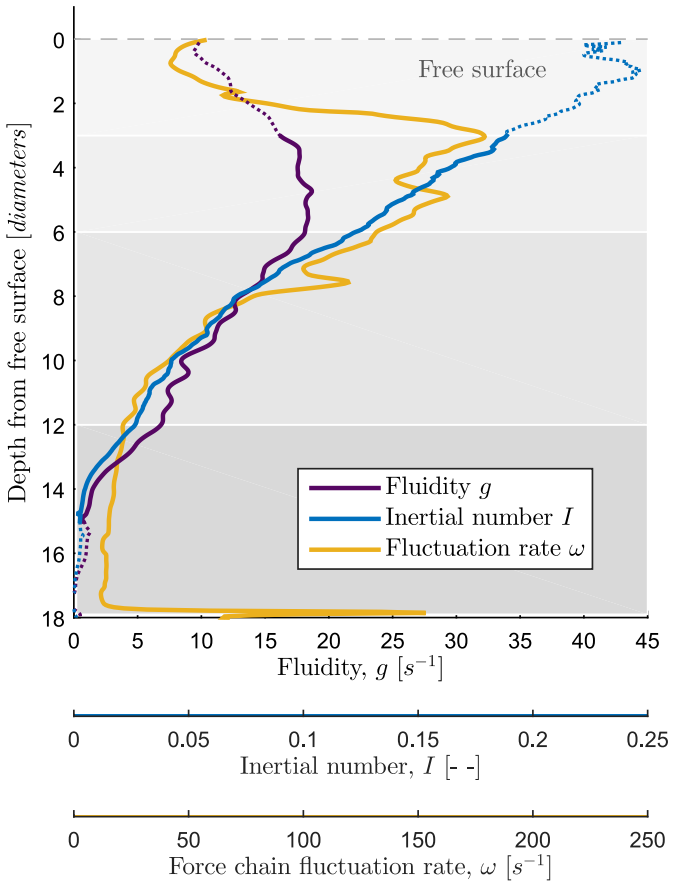

Fig. 9 Comparing three proposed definitions of fluidity: g, I, and ω. Each shaded region distinguishes the four flow regimes described in the text, from quasi-static (bottom) to nearly-collisional (top).

packed substrate, they observed no particle rearrangements, but their results had important implications for our understanding of bed entrainment. In fact, in our experiments discrete particle rearrangement events[66] are rare within the super-stable heap, but they undeniably exist. The significance of this is that we measure ω to be non-zero where there is creeping flow, even if no motion is observable for the duration of a single experimental run.

Non-local models originally extended the fluidity to regions where non-local effects were empirically observed. Only recently have microscopic definitions for granular fluidity been proposed, including strain-rate[34] and velocity fluctuations[35]. Indeed, the photoelastic response we measure as pixel intensities is due to strains both within the particles and at the contacts between two discs. This links the observed photoelastic responses to displacements of order smaller than a millimetre, and ω is related to fluctuations in particle velocities. As we interpret Figure 9, the force network fluctuation rate would capture where particles *may* flow, in both local and non-local regimes. Therefore, we propose ω is a local indicator of the susceptibility of a granular system to flow, and an indicator of granular fluidity in quasi-static state.

We notice that within depths of $6d - 12d$, where the flow is in the dense inertial regime, all three variables, g, ω and I are proportional to each other. They may therefore be expected to be interchangeable as measures of fluidity in the models for dense flows. However, I is easy to measure and a universally valid representation of fluidity for flows in dense inertial regime.

In the flowing layer, we are faced with two problems when interpreting Figure 9. First, up to a depth of $3d$ below the free surface, besides involving forces that are mostly weaker than the technique sensitivity, pixel intensity fluctuations are small at times where the flow thickness is smaller than the average. In this region, measurements for ω based on photoelasticity are therefore underestimated. Secondly, we need to consider the effect of changes in packing fraction on ω. Because the shear rate decreases towards the free surface above depths of $6d$ while μ is constant, so does g. Only I continues to increase all the way up to the free surface, but we attribute this to our underestimation of the pressure obtained from coarse-grained photoelastic measurements. In the transition to a collisional state, we suspect ω, I and g will no longer be proportional to each other. While such measurements are not accessible to us in our current set of data, Figure 9 raises the interesting question of how ω behaves in the dilute limit.

We propose that the force network fluctuation rate ω is a local indicator of the likelihood of flow. We suggest ω is an appropriate descriptor of granular fluidity in both quasi-static and dense inertial regimes. Nonetheless, we suspect that ω should depend on the packing fraction, so it would be interesting to investigate how it behaves in the transition to the collisional regime.

5 Conclusions

In this paper we report results of an experiment in which we applied photoelastic techniques to measure the dynamic interparticle forces within the bulk of a 2D avalanche. The flows investigated are in the dense, intermediate-I regime, flowing over an inclined layer of quasi-static discs. This provides insight into the dynamics near the boundary between dense inertial and quasi-static regimes. We find that the stress ratio $\mu = \tau/P$ is approximately constant within the dense flow, which is consistent with our expectation for a steady regime based on momentum conservation. The value of μ decreases slightly where the static layer begins near the bottom of the flow, but does not drop below the yield criterion μ_s. The resulting relationship between the μ and the inertial number I can be described by the local rheological model proposed by Jop *et al.* [12] (Eq. 4).

We use the experimental image pixel intensities forming the photoelastic patterns to define the force chain average fluctuation rate ω. Using these measurements we validate that there is a monotonic relationship between $\dot{\gamma}$ and ω[31] for flows in intermediate-I regime. However, Figure 6 suggests this proportionality breaks down for small shear rates. We hypothesize that this may be due to differences in magnitude of the force fluctuations in normal and shear directions for values of the stress ratio close to the yield criterion. Because in a quasi-static state rearrangement events[66] are infrequent, velocity and shear rate measurements may be underestimated, and so may the definitions of fluidity based on V_x and $\dot{\gamma}$. On the other hand, we interpret that $\omega > 0$ indicates regions where particles *may* flow, so we observe

$\omega > 0$ even within the quasi-static layer. The force network rearranges even where particles lie practically stationary, although such rearrangements are less frequent further from the boundary with the flowing layer.

This elucidates why non-local models[1,3] relied on the notion of stress diffusion to empirically extend the granular fluidity into regions where $\dot{\gamma} = 0$. Our results suggest that ω may provide a universal local quantification of the susceptibility of flow, and therefore may be a local variable that underlies granular fluidity, especially for quasi-static and low-I regimes. This interpretation complements the use of strain-rate and/or velocity fluctuations as measures of granular fluidity in the quasi-static regime. In particular, the photoelastic response creates a measureable signal in response to minuscule displacements (in fact smaller than could be measured with confidence for velocity fluctuations, as characterized by Xu *et al.* [67]). In this way, ω provides an experimentally-approachable measurement technique. Moreover, while a change in particle positions will cause a change in the forces, there are many valid configurations of forces for any one set of positions (the "force network ensemble"[36,37]). Since the forces set the yield criterion, we propose that their dynamics are an important control on fluidity, beyond simply the fluctuations in particle positions or velocities. Furthermore, in the dense-inertial regime where strain-rates and velocity fluctuations may be hidden in the larger-scale motions of the flow, ω is still easily measurable and scales with g and I.

A caveat against using ω is the sensitivity of the technique, which causes measurements to be underestimated near the free-surface. In addition, the results shown in this region raise the question of how changes in packing fraction affect the force fluctuation rate, and whether ω is a good descriptor of the susceptibility of flow in the dilute limit at all. Moreover, it would be interesting to further investigate how ω compares to the decoupled isotropic and anisotropic stress fluctuations, as well as the correlations between ω, I, shear and strain rate and velocity fluctuations in experiments where our discs can be observed at much higher resolution.

Another important implication of our measurement of ω is the potential use of the photoelastic technique to characterise the depth into the super-stable heap to which the flow may creep. If similar experiments were carried out over a deeper quasi-static region, then we propose that the depth at which $\omega = 0$ can be related to the *cooperative length* used in nonlocal models.

6 Conflicts of interest

There are no conflicts to declare.

7 Acknowledgements

We appreciate discussions with Michael Shearer about coarse-graining functions and with Jonathan Kollmer for his support in the use of PeGS. We thank Michel Louge, Ken Kamrin and the anonymous reviewers for their insights into the interpretation of our results. We are also very thankful to technicians David Page-Croft, Paul Mitton, Colin Hitch, Andrew Denson and John Milton for their invaluable help and technical support in the construction and maintenance of the experimental apparatus. This work is funded by IFPRI, NSF DMR 1206808, Dorothy Hodgkin Fellowship DH120121, Royal Society research grant RG130403, and the Cambridge International Trust.

References

1 K. Kamrin and G. Koval, *Physical Review Letters*, 2012, **108**, 178301.
2 M. Bouzid, M. Trulsson, P. Claudin, E. Clément and B. Andreotti, *Physical Review Letters*, 2013, **111**, 238301.
3 M. Bouzid, A. Izzet, M. Trulsson, E. Clément, P. Claudin and B. Andreotti, *The European Physical Journal E*, 2015, **38**, 125.
4 S. B. Savage, *Studies in Applied Mechanics*, Elsevier, 1983, vol. 7, pp. 261–282.
5 P. C. Johnson and R. Jackson, *Journal of Fluid Mechanics*, 1987, **176**, 67–93.
6 C. S. Campbell, *Annual Review of Fluid Mechanics*, 1990, **22**, 57–90.
7 J. T. Jenkins, *Physics of Fluids*, 2006, **18**, 103307.
8 Y. Forterre and O. Pouliquen, *Annual Review of Fluid Mechanics*, 2008, **40**, 1–24.
9 F. Da Cruz, S. Emam, M. Prochnow, J.-N. Roux and F. Chevoir, *Physical Review E*, 2005, **72**, 021309.
10 F. Chevoir, J. Roux, F. da Cruz, P. G. Rognon and G. Koval Jr, *Powder Technology*, 2009, **190**, 264–268.
11 G. MiDi, *The European Physical Journal E*, 2004, **14**, 341–365.
12 P. Jop, Y. Forterre and O. Pouliquen, *Nature*, 2006, **441**, 727.
13 R. Lespiat, S. Cohen-Addad and R. Höhler, *Physical Review Letters*, 2011, **106**, 148302.
14 J. Goyon, A. Colin, G. Ovarlez, A. Ajdari and L. Bocquet, *Nature*, 2008, **454**, 84.
15 P. D. Olmsted, *Rheologica Acta*, 2008, **47**, 283–300.
16 P. Richard, A. Valance, J. F. Métayer, P. Sanchez, J. Crassous, M. Louge and R. Delannay, *Physical Review Letters*, 2008, **101**, 248002.
17 O. Pouliquen, *Physics of Fluids*, 1999, **11**, 542–548.
18 W. A. Beverloo, H. A. Leniger and J. Van de Velde, *Chemical Engineering Science*, 1961, **15**, 260–269.
19 H. G. Sheldon and D. J. Durian, *Granular Matter*, 2010, **12**, 579–585.
20 K. Nichol, A. Zanin, R. Bastien, E. Wandersman and M. van Hecke, *Physical Review Letters*, 2010, **104**, 078302.
21 K. Reddy, Y. Forterre and O. Pouliquen, *Physical Review Letters*, 2011, **106**, 108301.
22 P. Mills, D. Loggia and M. Tixier, *Europhysics Letters*, 1999, **45**, 733.
23 L. S. Mohan, K. K. Rao and P. R. Nott, *Journal of Fluid Mechanics*, 2002, **457**, 377–409.
24 P. R. Nott, EPJ Web of Conferences, 2017, p. 11015.
25 P. G. Rognon, T. Miller, B. Metzger and I. Einav, *Journal of Fluid Mechanics*, 2015, **764**, 171–192.
26 P. Kharel and P. Rognon, *Europhysics Letters*, 2018, **124**, 24002.

27 D. L. Henann and K. Kamrin, *Physical Review Letters*, 2014, **113**, 178001.

28 K. Kamrin and D. L. Henann, *Soft Matter*, 2015, **11**, 179–185.

29 S. Li and D. L. Henann, *Journal of Fluid Mechanics*, 2019, **871**, 799–830.

30 T. Barker, D. G. Schaeffer, M. Shearer and J. M. N. T. Gray, *Proceedings of the Royal Society A*, 2017, **473**, 20160846.

31 O. Pouliquen and Y. Forterre, *Philosophical Transactions of the Royal Society of London A*, 2009, **367**, 5091–5107.

32 J. Zheng, A. Sun, Y. Wang and J. Zhang, *Physical Review Letters*, 2018, **121**, 248001.

33 R. A. Bagnold, *Proceedings of the Royal Society of London. Series A. Mathematical and Physical Sciences*, 1966, **295**, 219–232.

34 P. Jop, V. Mansard, P. Chaudhuri, L. Bocquet and A. Colin, *Physical Review Letters*, 2012, **108**, 148301.

35 Q. Zhang and K. Kamrin, *Physical Review Letters*, 2017, **118**, 058001.

36 J. H. Snoeijer, T. J. Vlugt, M. van Hecke and W. van Saarloos, *Physical Review Letters*, 2004, **92**, 054302.

37 J. E. Kollmer and K. E. Daniels, *Soft Matter*, 2019, **15**, 1793–1798.

38 A. L. Thomas and N. M. Vriend, *Physical Review E*, 2019, **100**, 012902.

39 J. E. Kollmer, *Photoelastic Grain Solver: https://github.com/jekollmer/pegs*, `https://github.com/jekollmer/pegs`.

40 K. E. Daniels, J. E. Kollmer and J. G. Puckett, *Review of Scientific Instruments*, 2017, **88**, 051808.

41 Z. Tang, T. A. Brzinski, M. Shearer and K. E. Daniels, *Soft Matter*, 2018, **14**, 3040–3048.

42 J. Barés, *Photoelastic methods: https://git-xen.lmgc.univ-montp2.fr/PhotoElasticity/Main/wikis/home*, `https://git-xen.lmgc.univ-montp2.fr/PhotoElasticity/Main/wikis/home`.

43 J. Barés, D. Wang, D. Wang, T. Bertrand, C. S. O'Hern and R. P. Behringer, *Physical Review E*, 2017, **95**, 052902.

44 A. Abed Zadeh, J. Barés, T. A. Brzinski, K. E. Daniels, J. Dijksman, N. Docquier, H. Everitt, J. E. Kollmer, O. Lantsoght, D. Wang *et al.*, *Granular Matter (in press) and arXiv:1902.11213*, 2019.

45 *Clear Flex 50 Series; Technical Data Sheet*, `https://www.smooth-on.com/tb/files/CLEAR_FLEX_50_95_TB.pdf`.

46 A. Favier de Coulomb, M. Bouzid, P. Claudin, E. Clément and B. Andreotti, *Physical Review Fluids*, 2017, **2**, 102301.

47 Y. Zhou, P. Ruyer and P. Aussillous, *Physical Review E*, 2015, **92**, 062204.

48 E. G. Coker and L. N. G. Filon, *A treatise on photoelasticity*, Cambridge University Press, 1931.

49 I. Goldhirsch, *Granular Matter*, 2010, **12**, 239–252.

50 T. Weinhart, A. R. Thornton, S. Luding and O. Bokhove, *Granular Matter*, 2012, **14**, 289–294.

51 K. W. Desmond and E. R. Weeks, *Physical Review E*, 2009, **80**, 051305.

52 S. Meyer, C. Song, Y. Jin, K. Wang and H. A. Makse, *Physica A: Statistical Mechanics and its Applications*, 2010, **389**, 5137–5144.

53 M. Y. Louge, A. Valance, P. Lancelot, R. Delannay and O. Artières, *Physical Review E*, 2015, **92**, 022204.

54 T. Weinhart, R. Hartkamp, A. R. Thornton and S. Luding, *Physics of Fluids*, 2013, **25**, 070605.

55 M. Y. Louge, *Physical Review E*, 2003, **67**, 061303.

56 N. Taberlet, P. Richard, A. Valance, W. Losert, J. M. Pasini, J. T. Jenkins and R. Delannay, *Physical Review Letters*, 2003, **91**, 264301.

57 Y. Grasselli and H. J. Herrmann, *Physica A: Statistical Mechanics and its Applications*, 1997, **246**, 301–312.

58 S. C. Du Pont, P. Gondret, B. Perrin and M. Rabaud, *Europhysics Letters*, 2003, **61**, 492.

59 R. Delannay, M. Louge, P. Richard, N. Taberlet and A. Valance, *Nature Materials*, 2007, **6**, 99.

60 R. Artoni and P. Richard, *Physical Review Letters*, 2015, **115**, 158001.

61 P. Jop, Y. Forterre and O. Pouliquen, *Journal of Fluid Mechanics*, 2005, **541**, 167–192.

62 L. Sarno, L. Carleo, M. N. Papa and P. Villani, *Rock Mechanics and Rock Engineering*, 2018, **51**, 203–225.

63 D. Howell, R. P. Behringer and C. Veje, *Physical Review Letters*, 1999, **82**, 5241.

64 S. Chialvo, J. Sun and S. Sundaresan, *Physical Review E*, 2012, **85**, 021305.

65 J. Estep and J. Dufek, *Journal of Geophysical Research: Earth Surface*, 2012, **117**, F1.

66 M. L. Falk and J. S. Langer, *Physical Review E*, 1998, **57**, 7192.

67 H. Xu, A. P. Reeves and M. Y. Louge, *Review of Scientific Instruments*, 2004, **75**, 811–819.